Wrinkling, creasing, and folding in fiber-reinforced soft tissues

Article *in* Extreme Mechanics Letters · November 2015

DOI: 10.1016/j.eml.2015.10.005

5 authors, including:

Peter S. Stewart

University of Glasgow

24 PUBLICATIONS **78** CITATIONS

SEE PROFILE

Sarah Waters

University of Oxford

113 PUBLICATIONS **1,276** CITATIONS

SEE PROFILE

Tamer Elsayed

Undisclosed

39 PUBLICATIONS **294** CITATIONS

SEE PROFILE

Dominic Vella

University of Oxford

97 PUBLICATIONS **1,237** CITATIONS

SEE PROFILE

Extreme Mechanics Letters manuscript No.
(will be inserted by the editor)

Wrinkling, creasing, and folding in fiber-reinforced soft tissues

Peter S. Stewart · Sarah L. Waters · Tamer El Sayed · Dominic Vella · Alain Goriely

October 30, 2015

Abstract Many biological tissues develop elaborate folds during growth and development. The onset of this folding is often understood in relation to the creasing and wrinkling of a thin elastic layer that grows whilst attached to a large elastic foundation. In reality, many biological tissues are reinforced by fibres and so are intrinsically anisotropic. However, the correlation between the fiber directions and the pattern formed during growth is not well understood. Here, we consider the stability of a two-layer tissue composed of a thin hyperelastic strip adhered to an elastic half-space in which are embedded elastic fibers. The combined object is subject to a uniform compression and, at a critical value of this compression, buckles out of the plane — it wrinkles. We characterize the wrinkle wavelength at onset as a function of the fiber orientation both computationally and analytically and show that the onset of surface instability can be either promoted or inhibited as the fiber stiffness increases, depending on the fibre angle. However, we find that the structure of the resulting folds is approximately independent of the fiber orientation. We also explore numerically the formation of large creases in fiber-reinforced tissue in the post-buckling regime.

Keywords creasing · wrinkling · constitutive modelling · fiber-reinforced materials

P. S. Stewart
School of Mathematics and Statistics, University of Glasgow, G12 8QW, UK

S. L. Waters, D. Vella, A. Goriely
Mathematical Institute, University of Oxford, OX2 6GG, UK, E-mail: goriely@maths.ox.ac.uk

T. El Sayed
Officio Kft., Toberek utca 5, 1112 Budapest, Hungary

1 Introduction

In recent years there has been considerable interest in the pattern created by the growth of a thin elastic layer attached to an elastic foundation [23]. The generic behaviour of such systems is to respond to a mismatch in stresses between the two layers by wrinkling (so that stress can be relaxed in the stiffer layer). However, the development of this wrinkling pattern beyond the onset of instability is surprisingly intricate: for large ratios of layer μ_l to foundation μ_s stiffness, $\mu_l/\mu_s \gtrsim 10$, a period-doubling instability occurs [5,7,6] due to nonlinearities in the substrate response. For small ratios of layer to foundation stiffness, $\mu_l/\mu_s \lesssim 10$, the system instead localizes the deformation and a fold or crease develops. For many biological systems, it is the latter scenario that is of most interest; for example, the deep folding patterns that are formed during the growth of brains are believed to be partially caused by this instability [11,13,17].

While the elastic instability of a growing multilayer material gives rise to wrinkling and folding patterns that appear similar to those observed *in vivo*, the material that makes up the white matter of the brain is known to be highly anisotropic, consisting of pre-stretched, axonal fiber bundles [26,19]. It is not clear whether and how this anisotropy might impact the relatively simple elastic behaviour discussed above. Studies in developing chick embryos [29] indicate that the fibrous structure is relatively passive and, further, that the fiber orientation is a consequence of the folding pattern, rather than its cause. Similarly, many other biological tissues are reinforced with collagen fibers, such as tendons and ligaments [27], annulus fibrosus in the spinal cord [18] and arterial walls [20,12,14].

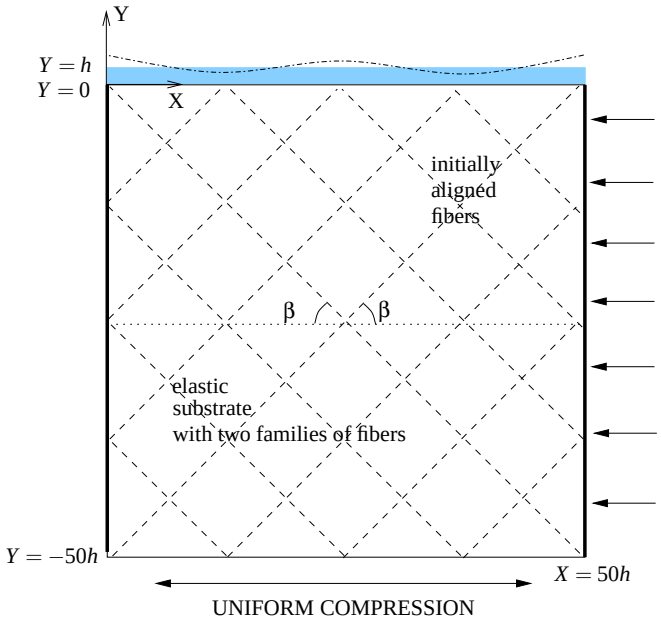

Fig. 1 Setup of the mathematical model.

In this paper we consider a model system that is motivated by the various tissues in the brain during development: a slab of homogeneous elastic tissue (representing the white matter) is connected to a thin layer of a stiffer tissue (representing the cerebral cortex). The setup is shown schematically in Fig. 1 and is similar in spirit to other models of cerebral cortex folding [1,23,4]. In each region, we assume that the material is elastic with reinforced fibers and a fiber pre-stretch. We study the influence of the fiber orientation and of the pre-stretch by direct computational simulations. We then compare these results with those of a linear stability analysis.

2 The model

In the reference configuration, the two-layer material is described by the coordinates $\mathbf{X} = (X, Y, Z)$, shown in Fig. 1, with the interface between the two layers is denoted $Y = 0$. Deformation of the tissue to a new configuration parametrized by current coordinates $\mathbf{x} = (x, y, z)$, is described by the mapping $\mathbf{x} = \chi(\mathbf{X}, t)$, where t is time, with corresponding deformation gradient tensor $\mathbf{F}(\mathbf{X}, t)$. Both layers of tissue are assumed hyperelastic, and can be described by strain energy functions $\mathcal{W}_l(\mathbf{F})$ and $\mathcal{W}_s(\mathbf{F})$, for the upper layer and the substrate, respectively. We assume that the deformation occurs sufficiently slowly that inertial effects can be neglected and that the strain lies in the (X, Y)-plane.

The upper layer is modeled as a neo-Hookean material of uniform thickness H with shear modulus μ_l and bulk modulus K_l, i.e.

$$\mathcal{W}_l = \mu_l(\overline{\lambda}_1^2 + \overline{\lambda}_2^2 + \overline{\lambda}_3^2 - 3) + \tfrac{1}{2}K_l \log J, \tag{1}$$

where $J = \det(\mathbf{F})$ and $\overline{\lambda}_j$ are the principal values of the left Cauchy-Green tensor $\overline{\mathbf{F}}^{\mathrm{T}}\overline{\mathbf{F}}$, where $\overline{\mathbf{F}} = J^{-1/3}\mathbf{F}$. The material is modeled as a standard fiber-reinforced material. That is, the substrate is modeled as a neo-Hookean elastic half-space, in the region $Y < 0$. This half space contains two families of fibers which are assumed to contribute to the strain-energy density at the lowest possible positive powers in the fiber strain. For simplicity, we assume that the matrix and fibers experience the same deformation gradient, so the energy of the substrate may thus be written using an additive decomposition in the form $\mathcal{W}_s = \varphi_m\mathcal{W}_m + \varphi_f\mathcal{W}_f$ where

$$\mathcal{W}_m = \mu_s(\overline{\lambda}_1^2 + \overline{\lambda}_2^2 + \overline{\lambda}_3^2 - 3) + \tfrac{1}{2}K_s \log J, \tag{2}$$

$$\mathcal{W}_f = \sum_{i=1}^{2} f(I_4^{(i)}), \qquad f(\eta) = \frac{\mu_f}{4}(\eta - {\lambda_f}^2)^2. \tag{3}$$

Here φ_f and φ_m represents the volume fractions of all fibers and matrix, respectively, while

$$I_4^{(i)} = (\mathbf{N}^{(i)})^{\mathrm{T}}\mathbf{F}^{\mathrm{T}}\mathbf{F}\mathbf{N}^{(i)}, \quad (i = 1, 2),$$

where the unit vector $\mathbf{N}^{(i)}$ $(i = 1, 2)$ is the direction in which fiber family $i)$ is aligned in the reference configuration. We have therefore assumed that the fibers are equal and opposite (with angle $\pm\beta$ with the X-direction). Finally, λ_f is the fiber-prestress, which is assumed constant. For $\lambda_f < 1$, the fibers are under tension in the reference configuration. It should be noted that this constitutive model allows the fibers to bear compressive loading [15], which is usually neglected when modeling tissues reinforced by collagen fibers such as arteries [12].

We non-dimensionalize all lengths by the thickness of the upper layer, H, and all moduli by μ_s, i.e. we take $\mu_s = 1$ without loss of generality. Using a Poisson ratio for both layers of approximately 0.35 [8], we take the bulk moduli $K_s \approx 3$, $K_l \approx 3\mu_l$. The values of other fixed parameters are based on those relevant for brain tissues and are given in Table 1.

Growth of the material is mimicked by uniform compression of the two-layer material parallel to the X direction. The key parameter controlling this compression is the end–shortening $d = \Delta L/L$

2.1 Methods

The model is solved implicitly using an ABAQUS UMAT, which for a given deformation gradient tensor $\mathbf{F}$ requires both the corresponding Cauchy stress tensor $\boldsymbol{\sigma}$

variable	symbol	benchmark value
fiber volume fraction	φ_f	0.1
matrix volume fraction	φ_m	0.9
upper layer bulk modulus	K_l	$3\mu_l$=30
substrate bulk modulus	K_s	3
upper layer shear modulus	μ_l	10
fiber-stiffness	μ_f	10
fiber pre-stretch	λ_f	1.0

Table 1 Benchmark parameters used in the computational simulations. All moduli are dimensionless

and a stiffness tensor $\mathbf{C}$. The first Piola stress tensor for the neo-Hookean component of each layer is computed using a predictor-corrector method used previously by [10], based on the nonlinear viscoelastic formulation of [24]. For the substrate we then additively combine this with the Piola stress obtained analytically from (3). Given the first Piola stress tensor for each layer, we then easily push forward to compute the total Cauchy stress $\boldsymbol{\sigma}$.

For computational purposes we consider a truncated half-space in three spatial dimensions: the dimensionless planar coordinates X, Y, Z satisfying $-50 \leq X \leq 50$, $-50 \leq Y \leq 0$, $0 \leq Z \leq 1$. Along $Y = -50$, we apply a condition of no component of the displacement perpendicular to the direction compression. We further truncate the X direction by applying symmetry boundary conditions along the centre of the domain ($X = 0$); this reduces the computational cost of individual simulations. To ensure the deformations exhibit strain in the (X, Y) plane alone we impose no-displacement conditions in the Z direction along $Z = 0$ and $Z = 1$.

We benchmark our numerical implementation by considering the homogeneous compression of the two-layer material. This deformation takes the simple form, $\mathbf{x} = (\lambda_1 X, \lambda_{2,j} Y)$, $(j = l, s)$. In a state of simple compression, both layers of the material must experience zero normal stress on their interfaces perpendicular to the direction of compression, which is possible only if

$$\varphi_m \left(\frac{\frac{2}{3}\lambda_{2,s}^2 - \frac{1}{3}(\lambda_1^2+1)}{(\lambda_1\lambda_{2,s})^{5/3}} + K_s \frac{\log(\lambda_1\lambda_{2,s})}{\lambda_1\lambda_{2,s}} \right),$$

$$+ 4\varphi_f \sin^2\beta \frac{\lambda_{2,s}}{\lambda_1} f'\left(\lambda_1^2\cos^2\beta + \lambda_{2,s}^2\sin^2\beta\right) = 0, \quad (4a)$$

$$\mu_l \frac{\frac{2}{3}\lambda_{2,l}^2 - \frac{1}{3}(\lambda_1^2+1)}{(\lambda_1\lambda_{2,l})^{5/3}} + K_l \frac{\log(\lambda_1\lambda_{2,l})}{\lambda_1\lambda_{2,l}} = 0. \quad (4b)$$

Given a compression in the X direction, λ_1, the stretches in the Y direction for each layer are determined by (4a) and (4b) (cf. the Poisson effect in a uniaxially stretched bar). The resulting substrate stretch $\lambda_{2,s}$ (determined from 4a) is plotted in Fig. 2 as a function of the applied compression λ_1. The corresponding results of our simulations are shown as open circles and are seen to be in excellent agreement with that predicted by (4a). Note that if both materials are assumed incompressible, we have $\lambda_{2,l} = \lambda_{2,s} = 1/\lambda_1$ (shown as the dashed curve in Fig. 2).

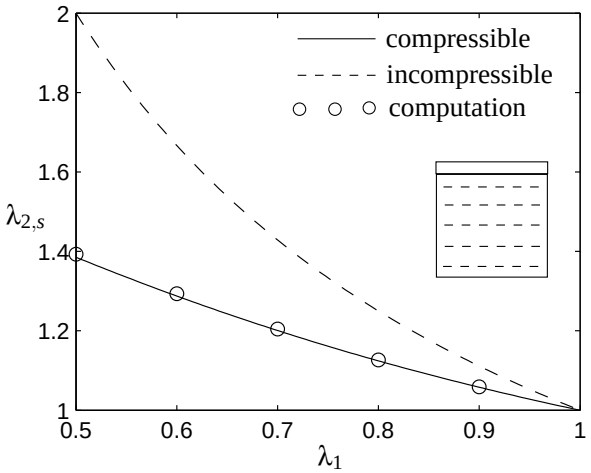

Fig. 2 Normal stretch induced in the substrate, $\lambda_{2,s}$, by a homogeneous uniaxial deformation λ_1 in the X direction. Here, the predictions of (4a) are shown for both compressible (solid curve) and incompressible (dashed curve) materials; the results from numerical simulations are shown for the compressible case only (circles). In each case the fibers are horizontal ($\beta = 0$), and other parameters are as listed in Table 1.

Next, we consider the stability of a small perturbation to this state of simple compression. Computationally, we apply the compression in three distinct stages [25]: first, we uniformly displace the material boundary at $X = 50$ towards $X = 0$ by 0.5% of the ultimate compression, d; second, we apply a sinusoidal perturbation to the upper interface as a prescribed displacement, using a combination of cosine modes with an integer number of wavelengths N across the domain, where the total amplitude of the free surface at $X = 0$ is denoted A_{init}; third, the material is compressed to the full value of the displacement d. In addition, we consider the stability of the homogeneous state by constructing an analytical model similar to the work of Biot [2,3]; this is discussed in Appendix A.

3 Results

We begin by considering the onset of (wrinkling) instability as a function of the fiber properties, before progressing to consider the development of large amplitude creases. Benchmark parameters for our model are listed in Table 1.

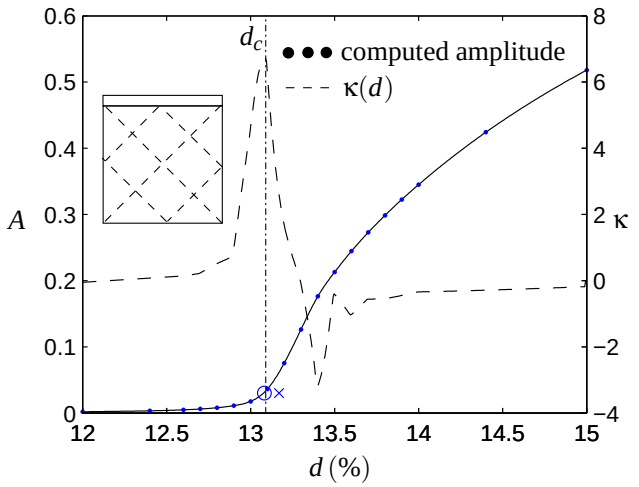

Fig. 3 Amplitude of the final surface pattern A as a function of the applied displacement d. Computed points are shown as filled blue circles (joined by line segments to illustrate the trend). The curvature of $A = A(d)$ at a given d, denoted κ, is interpolated from the computed points and is shown as a dashed curve. The open circle and vertical line show the computed compression at which maximal curvature should occur, $d = d_c$; the cross shows the critical compression predicted on the basis of the linear theory. Here $\beta = \pi/4$ and other parameters are as in Table 1.

3.1 Onset of surface patterning

We investigate the onset of patterning using an initial surface perturbation of wavenumber k with total amplitude $A_{\text{init}} = 0.05$ and measure the final amplitude of the pattern A. Changes to the initial amplitude made no appreciable difference to the computational results. To quantify the onset of wrinkling instability on the surface of the tissue, we illustrate a typical example by plotting the amplitude of the surface pattern, A, as a function of the applied displacement, d, in Fig. 3 for initial fiber angle $\beta = \pi/4$. This plot can be approximately divided into two parts: an inner curve in the region $0 < d < d_c$, where the growth of the perturbation is very small (approximately linear in d), and an outer curve in the region $d > d_c$, where the amplitude increases rapidly behaving like $(d-d_c)^{1/2}$ close to onset. In the neighbourhood of this change, we note that the function $A = A(d)$ is highly curved. We therefore compute the curvature $\kappa = A''(d)/[1 + (A')^2]^{3/2}$ and plot this as the dashed curve in Fig. 3. The critical value of d at the changeover, $d = d_c$, is taken to be the value that maximizes κ and is shown as an open circle on the example illustrated in Fig. 3. The results of an analytical linear stability analysis (Appendix A) predict a slightly different critical compression, shown as a cross in Fig. 3. We hypothesise that this difference arises due to either finite-size effects or the difficulty in determining the exact point of bifurcation from the numerical computations.

The bifurcation diagram shown in Fig. 3 is qualitatively similar to that found throughout the parameter space. The key parameter that varies is the value of d_c. Fig. 4 illustrates that the value of d_c depends on both the wavenumber of the imposed perturbation and the initial fiber orientation. In particular, the results obtained with perturbations with either $N = 4$, $N = 5$ or $N = 6$ wavelengths across the computational domain are shown in Fig. 4(a). These correspond to the three most unstable modes in all cases tested and demonstrate that instability occurs through wrinkling with a well-defined wavelength. In each case, the analytical theory (Appendix A) gives a prediction for d_c at a given wavenumber k (though since this calculation assumes an infinite domain, k is allowed to vary continuously). The analytical predictions for each initial fiber angle are shown as solid curves in Fig. 4(a) and demonstrate excellent agreement with the computations. Furthermore, we note that the fiber orientation β has a significant effect on the value of the critical compression at which wrinkling occurs: d_c changes by $\approx 50\%$ as β increases from 0 to $\pi/2$.

For each fiber orientation β the predicted onset curve, $d_c(k)$, exhibits a local minimum: there is a smallest compression at which a wrinkled solution with growing amplitude exists. The wavenumber at this minimum critical compression is denoted k_0 and is expected to be the wavenumber that is observed at the onset of wrinkling as the compression d is increased. To quantify how this wavenumber varies with the fiber angle, we plot k_0 as a function of β in Fig. 4(b) for several fiber stiffnesses μ_f. Variations in the initial fiber angle result in a range of admissible onset wavenumbers $k_{min} < k_0 < k_{max}$. Each curve in Fig. 4(b) is non-monotonic in β and the curves are similar in shape but with different amplitudes; the minimal critical wavenumber (k_{min}) is attained with fibers aligned to the direction of compression ($\beta = 0$) while the maximal critical wavenumber is attained with an intermediate inclination angle $\beta \approx 1.18$. This non-monotonic behavior as function of the fiber angle is a typical feature of fiber-reinforced materials and is also found in reinforced cylindrical shells [16]. An interesting feature of Fig. 4(b) is the relatively modest changes in the selected wavenumber as the fiber angle and stiffness change. Even with very stiff fibers ($\mu_f = 20$), the onset wavenumber k_0 only varies by a maximum of 13.4% from the value predicted in the absence of the fibers. Another interesting feature of Fig. 4(b) is that the curves for different μ_f intersect for a particular value of $\beta = \beta_c \approx 0.3846$ with corresponding critical wavenumber $k_0 = k_c \approx 0.5516$

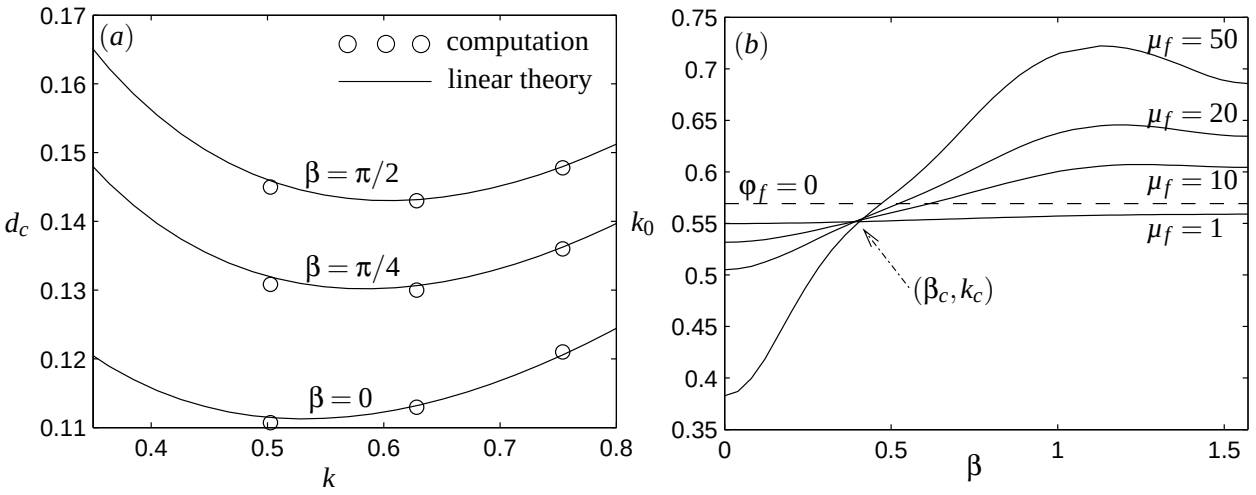

Fig. 4 (a) Critical compression required for instability, d_c, as a function of the wavenumber of the initial perturbation k for $\mu_f = 10$. The results of simulations (open circles) compare well with the predictions of the analytical theory (solid curve). Note that at a given value of β, d_c, is minimized at $k = k_0$; we therefore expect wrinkles with this wavenumber to emerge at the onset of instability as d is increased. (b) Theoretical prediction of the wavenumber at onset, k_0, as a function of the fiber angle β for several values of the fiber-stiffness $\mu_f = 1, 10, 20, 50$. Other parameters are as listed in Table 1. The horizontal dashed line corresponds to wavenumber at onset in the absence of fibres, $\varphi_m = 1$, $\varphi_f = 0$.

(marked on Fig. 4b); for $\beta = \beta_c$ the critical value of the wavenumber is independent of the fibre stiffness. To explain this observation we consider the critical threshold for wrinkling with two families of fibers setting $\mu_f = 0$ but holding the volume fraction of each family of fibers fixed at $\varphi_f = 0.05$. In this case we compute the critical compression for instability as $k_0 \approx 0.5515$, almost indistinguishable from the critical compression where the curves in Fig. 4(b) cross, k_c. Hence, for the fiber angle β_c the components of the stress due to the fibers cancel identically, mimicking a homogeneous material. We expect that the value of β_c will be a function of the volume fraction of each fiber family φ_f. It should also be noted that with no pre-stretch, for some angles β the fibers are compressed and thus may buckle, which would change the elastic properties of the substrate, but this possibility is not considered in this study.

In Fig. 5, we show the effect of the fiber stiffness on the critical compression. As expected, as the fibers become stiffer, the critical compression for wrinkling decreases for $\beta = 0$ and increases for $\beta = \pi/2$. Note that for $\mu_f = 50$ (for other parameters listed in Table 1), the difference in the critical compression required is very large which shows the importance of fibers in providing a stabilization or destabilization mechanism based on the fiber angle. We conclude that the fiber stiffness and orientation both influence the critical onset compression d_c for wrinkling instability, but that the onset wavelength is approximately independent of the fiber orientation Fig. 5.

To further assess the range of admissible wavenumbers for a particular fiber stiffness, Fig. 6(a) illustrates the maximal and minimal admissible wavenumbers of the instability (as β varies) for different values of the fiber stiffness μ_f. The range of admissible wavenumbers expands as the fiber stiffness increases, but the variation in surface wavelength remains small for these parameter values. For example, for $\mu_f = 20$ and $\mu_l = 10$ (all other parameters as in Table 1) the maximal observed wavelength (for $\beta \approx 1.18$) is only 1.15 times the minimal observed wavelength (for $\beta = 0$). With no fiber pre-stretch ($\lambda_f = 1$), under certain conditions (for example when the fibers are initially aligned along the direction of compression, $\beta = 0$) the fibers become highly compressed in the homogeneous state. However, axonal fibers in the brain grow under tension [31], which we incorporate into our model by decreasing the pre-stretch factor λ_f, as shown in Fig. 6(b). As the fiber pre-stretch increases the range of admissible wavenumbers is diminished, reducing the possible variation in surface wavelength due to the fibers. In summary, Fig. 6 illustrates that the range of admissible wavenumbers driven by the fibers is small and further contracted by increasing the fiber pre-stretch parameter.

3.2 Large-amplitude simulations

We now consider the nonlinear growth of these small-amplitude wrinkles into folds and creases. Under uniform compression, a surface can exhibit two modes of

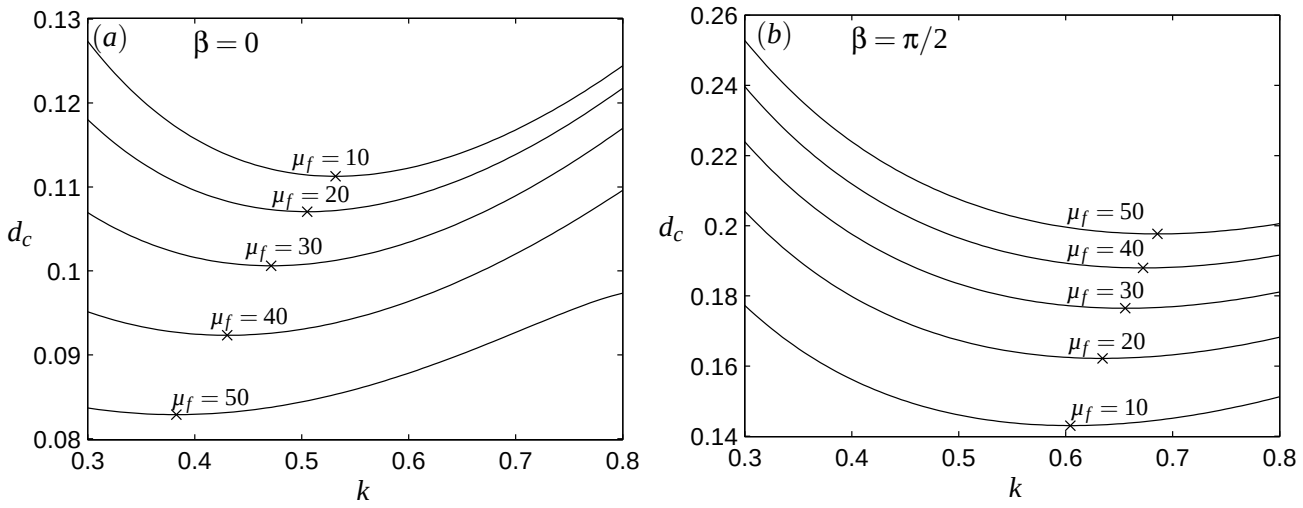

Fig. 5 Critical compression required for instability, d_c, as a function of the wavenumber of the initial perturbation k for two different fiber angles predicted from the analytical theory: (a) $\beta = 0$; (b) $\beta = \pi/2$. The $\times$ symbol represents the minimal compression required for the onset of instability. Parameters are as listed in Table 1.

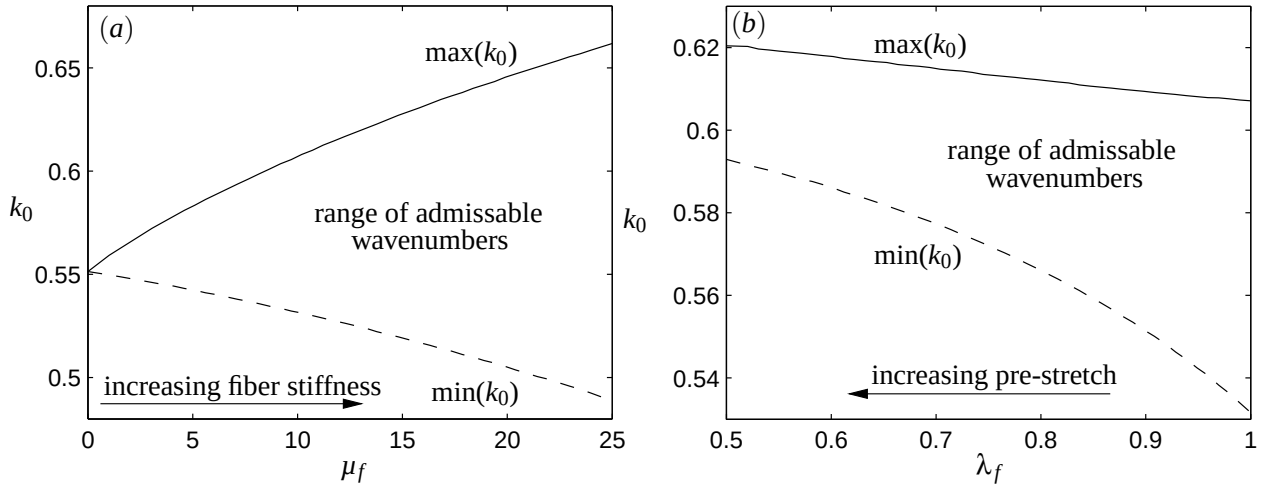

Fig. 6 Prediction from the linear theory for the admissible wavenumbers at onset (obtained as β varies): the onset wavenumber k_0 lies between k_{min} (dashed curves) and k_{max} (solid curves). The span of admissible wavenumbers is shown (a) for increasing fiber stiffness μ_f and (b) for increasing fiber pre-stretch λ_f. Other parameters are as given in Table 1.

patterning: a crease or a fold [22]. To capture the nonlinear growth in this system, we extend the procedure outlined in §3.1 to larger compressions. Across the parameter space a unified picture emerges, as illustrated in Fig. 7 for $\beta = \pi/4$. As compression increases with $d > d_c$, the wrinkled surface grows in amplitude (Fig. 7a) and stress builds up in the region around the local surface minima. As the compression continues, the tissue surface forms a cusp at the trough of the wrinkle and the interface makes contact with itself at $d \approx 0.4$ (Fig. 7b) at the local minimum of the trough. The no penetration conditions are enforced using 'hard' contact implemented in ABAQUS. Under further compression, the contact region 'zips up' and forms a crease (Fig. 7c). The qualitative behavior of the system was found to be independent of the initial fiber orientation (not shown), although the critical compression required for self-contact varies within a small range. In all cases tested we observe a wrinkle-to-crease transition in this system. A similar wrinkle-to-crease transition was previously observed by [28].

4 Discussion

Motivated by the folding of the cerebral cortex during neural development, we considered the instability of

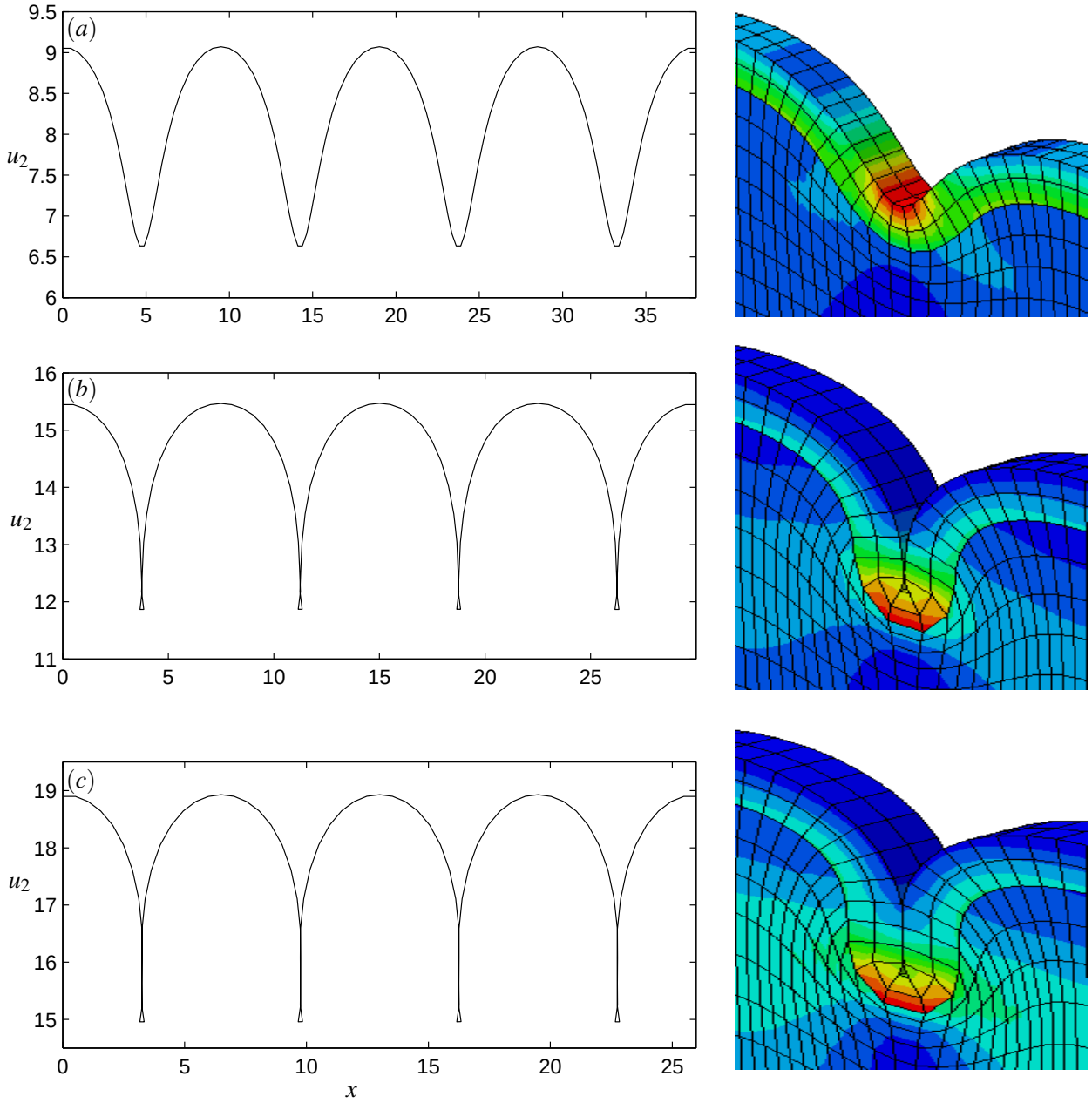

Fig. 7 Nonlinear growth of the fold for increasing compression to large compressions, showing the profile of the free surface on the LHS, and a three-dimensional projection of the computational domain on the RHS, where the shading corresponds to the von Mises stress: (a) $d = 0.24$; (b) $d = 0.4$; (c) $d = 0.48$. Here $\beta = \pi/4$, with other parameters given as in Table 1.

a two-layer continuum (mimicking the grey and white matter) under a uniform compression. This model explicitly included discrete families of elastic fibers within the substrate. Our aim was to characterize the influence of these fibers on the surface instability and folding. Each layer of tissue was modeled as a compressible neo-Hookean material, although our computational formulation extends easily to more sophisticated tissue models [9]. Throughout this study we have ignored both plastic deformation and viscoelastic relaxation of the tissue since the measured relaxation times for soft tissue (seconds) are typically much faster than the timescale of growth (weeks/months).

We used a simple model for the elastic fibers, assuming that they are homogeneously distributed across the white matter layer with constant shear modulus and pre-stress factor, initially aligned in an equal and opposite manner at some constant angle to the direction of compression. The model was solved using a combination of numerical simulations (§3) and analytic the-

ory (Appendix A), yielding a unified picture: the homogeneously compressed state becomes unstable above a critical compression, exhibiting a wrinkling instability whose amplitude grows as the compression increases (Fig. 3). The onset wavelength of this instability varies within a narrow window as a function of the initial fiber orientation (Fig. 4) expanding as a function of increasing fiber stiffness (Fig. 6a), but contracting as a function of increasing fiber prestress (Fig. 6b). Hence, fibers distributed homogeneously throughout the material do not significantly influence the folding pattern on the surface. However, the presence of fibers does have a significant effect on the critical compression at which instability is observed. Note that localized variation in fiber properties (such as U-fibers connecting regions in the same portion of the cortex) could have an influence the folding in a particular region; consideration of this possibility is deferred to future work.

As compression increases, the surface wrinkle grows in amplitude with a localized increase in stress at the trough (Fig. 7a). At some critical compression the surface exhibits a wrinkle-to-crease transition (Fig. 7), where the interface forms a cusp (discontinuous curvature) at the trough of the wrinkle; for further increases in the compression the contact surface enlarges from the trough forming a crease similar to those observed in single layer materials [22], but distinct from the elaborate surface folds observed when the upper layer is prestressed [25,30]. We therefore suggest that the transition between large amplitude creasing and folding may be driven by residual stress in the upper layer which could possibly be generated through differential growth of the two cortical layers.

Acknowledgements AG is a Wolfson/Royal Society Merit Award Holder and acknowledges support from a Reintegration Grant under EC Framework VII.

A Linear theory

Following [2], we consider of the linear stability of the two-layer material under uniform compression. For simplicity, we assume that the deformation is two-dimensional, similar to the analysis of [7] for a single material. We assume that both constituent phases are compressible neo-Hookean solids as described in the main text. The homogeneous basic state is given by (4) in the main paper. We perturb this state by expanding the deformed configuration in both layers (where the subscripts l and s denote the upper layer and the substrate, respectively, using the convention of Sect. 2) about the homogeneous state in the form,

$$\mathbf{x}_l^{(1)} = ((1-d)X, \lambda_{2,l}Y) + \epsilon \mathbf{U}_l(X,Y), \quad (0<Y<H), \tag{5a}$$
$$\mathbf{x}_s = ((1-d)X, \lambda_{2,s}Y) + \epsilon \mathbf{U}_s(X,Y), \quad (Y<0), \tag{5b}$$

respectively, where $\epsilon \ll 1$ is a small parameter.

Substituting this deformation into the strain energy for the upper layer (1), and applying the Euler-Lagrange equations results in governing equations of the form

$$a_{xx}U_{l,XX} + a_{yy}U_{l,YY} + a_{xy}V_{l,XY} = 0, \tag{6a}$$
$$b_{xx}V_{l,XX} + b_{yy}V_{l,YY} + b_{xy}U_{l,XY} = 0, \tag{6b}$$

where the constants take the form

$$a_{xx} = \lambda_{2,l}[(\lambda_1\lambda_{2,l})^{1/3}\mu_l(\tfrac{5}{9} + \tfrac{2}{9}\lambda_1^2 + \tfrac{5}{9}\lambda_{2,l}^2) + K_l\lambda_1\lambda_{2,l} - K_l\lambda_1\lambda_{2,l}\log(\lambda_1\lambda_{2,l})], \tag{6c}$$
$$a_{xy} = \lambda_1((\lambda_1\lambda_{2,l})^{1/3}\mu_l(\tfrac{5}{9} - \tfrac{1}{9}\lambda_1^2 - \tfrac{1}{9}\lambda_{2,l}^2) + K_l\lambda_1\lambda_{2,l} - K_l\lambda_1\lambda_{2,l}\log(\lambda_1\lambda_{2,l}))], \tag{6d}$$
$$a_{yy} = \mu_l\lambda_1^2\lambda_{2,l}[(\lambda_1\lambda_{2,l})^{1/3}], \tag{6e}$$
$$b_{xx} = \mu_l\lambda_1\lambda_{2,l}[(\lambda_1\lambda_{2,l})^{1/3}], \tag{6f}$$
$$b_{xy} = \lambda_{2,l}[(\lambda_1\lambda_{2,l})^{1/3}\mu_l(\tfrac{5}{9} - \tfrac{1}{9}\lambda_1^2 - \tfrac{1}{9}\lambda_{2,l}^2) + K_l\lambda_1\lambda_{2,l} - K_l\lambda_1\lambda_{2,l}\log(\lambda_1\lambda_{2,l})], \tag{6g}$$
$$b_{yy} = \lambda_1[(\lambda_1\lambda_{2,l})^{1/3}\mu_l(\tfrac{5}{9} + \tfrac{5}{9}\lambda_1^2 + \tfrac{2}{9}\lambda_{2,l}^2) + K_l\lambda_1\lambda_{2,l} - K_l\lambda_1\lambda_{2,l}\log(\lambda_1\lambda_{2,l})]. \tag{6h}$$

In a similar manner for the substrate (3), the extra constitutive model for the fibers increases the complexity of the coefficients, but the governing equations retain their overall structure in the form

$$c_{xx}U_{s,XX} + c_{yy}U_{s,YY} + c_{xy}V_{s,XY} = 0, \tag{6i}$$
$$d_{xx}V_{s,XX} + d_{yy}V_{s,YY} + d_{xy}U_{s,XY} = 0, \tag{6j}$$

where the constants take the form,

$$c_{xx} = \lambda_{2,s}[\varphi_m((\lambda_1\lambda_{2,s})^{1/3}(\tfrac{5}{9} + \tfrac{2}{9}\lambda_1^2 + \tfrac{5}{9}\lambda_{2,s}^2) + K_s\lambda_1\lambda_{2,s} - K_s\lambda_1\lambda_{2,s}\log(\lambda_1\lambda_{2,s})) \tag{6k}$$
$$+ 4\lambda_1^3\lambda_{2,s}\varphi_f\cos^2\beta f'(q) + 8\lambda_1^5\lambda_{2,s}\varphi_f\cos^4\beta f''(q)], \tag{6l}$$
$$c_{xy} = \lambda_1[\varphi_m((\lambda_1\lambda_{2,s})^{1/3}(\tfrac{5}{9} - \tfrac{1}{9}\lambda_1^2 - \tfrac{1}{9}\lambda_{2,s}^2) + K_s\lambda_1\lambda_{2,s} - K_s\lambda_1\lambda_{2,s}\log(\lambda_1\lambda_{2,s})) + 16\lambda_1^3\lambda_{2,s}^3\varphi_f\cos^2\beta\sin^2\beta f''(q)], \tag{6m}$$
$$c_{yy} = \lambda_1^2\lambda_{2,s}[(\lambda_1\lambda_{2,s})^{1/3}\varphi_m + 4\lambda_1\lambda_{2,s}\varphi_f\sin^2\beta f'(q) + 8\lambda_1^3\lambda_{2,s}\varphi_f\cos^2\beta\sin^2\beta f''(q)], \tag{6n}$$
$$d_{xx} = \lambda_1\lambda_{2,s}[(\lambda_1\lambda_{2,s})^{1/3}\varphi_m + 4\lambda_1\lambda_{2,s}\varphi_f\cos^2\beta f'(q) + 8\lambda_1\lambda_{2,s}^3\varphi_f\cos^2\beta\sin^2\beta f''(q))], \tag{6o}$$
$$d_{xy} = \lambda_{2,s}[(\varphi_m((\lambda_1\lambda_{2,s})^{1/3}(\tfrac{5}{9} - \tfrac{1}{9}\lambda_1^2 - \tfrac{1}{9}\lambda_{2,s}^2) + K_s\lambda_1\lambda_{2,s} - K_s\lambda_1\lambda_{2,s}\log(\lambda_1\lambda_{2,s})) + 16\lambda_1^3\lambda_{2,s}^3\varphi_f\cos^2\beta\sin^2\beta f''(q)], \tag{6p}$$
$$d_{yy} = \lambda_1[\varphi_m((\lambda_1\lambda_{2,s})^{1/3}(\tfrac{5}{9} + \tfrac{5}{9}\lambda_1^2 + \tfrac{2}{9}\lambda_{2,s}^2) + K_s\lambda_1\lambda_{2,s} - K_s\lambda_1\lambda_{2,s}\log(\lambda_1\lambda_{2,s})) + 4\lambda_1\lambda_{2,s}^3\varphi_f\sin^2\beta f'(q) + 8\lambda_1\lambda_{2,s}^5\varphi_f\sin^4\beta f''(q)], \tag{6q}$$

where

$$q = \lambda_1^2\cos^2\beta + \lambda_{2,l}^2\sin^2\beta. \tag{6r}$$

In both regions we look for solutions which are periodic in X, with wavenumber k, and exponentially decaying in $Y<0$, in the form

$$U_j(X,Y) = \overline{U}_j(kY)\sin(kX)\exp(ka_jY), \qquad (j=l,s) \tag{6s}$$
$$V_j(X,Y) = \overline{V}_j(kY)\cos(kX)\exp(ka_jY), \qquad (j=l,s). \tag{6t}$$

Substitution into (6a) results in a quartic polynomial with four roots $a_{l,m}$ $(m = 1, \cdots, 4)$ applicable to the cortex layer. Similarly, substitution into (6i) results in a quartic polynomial for the white matter, where we can immediately neglect the two roots with positive real part since these do not decay as $Y \to \infty$, leaving two roots $a_{s,1}$ and $a_{s,2}$. The polynomials themselves are very long and cumbersome, so we do not reproduce them here for brevity. We hence compute the corresponding eigenvectors $\mathbf{v}_{j,m} = (\overline{U}_j, \overline{V}_j)$ $(j = 1, 2)$ in both regions and then express the displacement vectors in both regions as an eigenfunction expansion in the form

$$\overline{\mathbf{U}}_s = A_1\mathbf{v}_1 \exp(a_{s,1}Y) + A_2\mathbf{v}_2 \exp(a_{s,2}Y), \quad (Y < 0) \quad (6u)$$

$$\overline{\mathbf{U}}_c = A_3\mathbf{v}_3 \exp(a_{l,1}Y) + A_4\mathbf{v}_4 \exp(a_{l,2}Y) + A_5\mathbf{v}_5 \exp(a_{u,3}Y) + A_6\mathbf{v}_6 \exp(a_{l,4}Y), \quad (0 < Y < 1), \quad (6v)$$

as a function of the vector of amplitudes $\mathbf{a} = (A_1, \ldots, A_6)$.

On the interface between the two layers $(Y = 0)$ we impose continuity of displacement and continuity of normal and tangential stress. Similarly, on the upper surface of the cortex $(Y = 1)$ we impose conditions of no normal and tangential stress. These can be combined into a matrix equation for the coefficients in the form $\mathbf{Ma} = \mathbf{0}$. Finally, we compute the critical compression required for the onset of instability as the value d_c for which $\det(\mathbf{M}) = 0$.

References

1. Bayly PV, Okamoto RJ, Xu G, Shi Y,Taber LA, A cortical folding model incorporating stress-dependent growth explains gyral wavelengths and stress patterns in the developing brain, Physical Biology, 10(1) 016005 (2013)
2. Biot MA, Folding instability of a layered viscoelastic medium under compression, Proceedings of the Royal Society of London. Series A. Mathematical and Physical Sciences, 242 (1231), 444-454 (1957)
3. Biot MA, Surface instability of rubber in compression, Applied Scientific Research, Section A, 12(2), 168-182 (1963)
4. Budday, S. and Steinmann, P. and Goriely, A. and Kuhl, E. Extreme Mechanics Letters (2015).
5. Brau F, Vandeparre H, Sabbah A, Poulard C, Boudaoud A, Damman P, Nature Phys., 7, 56–60 (2010)
6. Brau F, Damman P, Diamant H, Witten TA, Soft Matter, 9, 8177–8186 (2013)
7. Cao Y, Hutchinson JW, Wrinkling phenomena in neo-Hookean film/substrate bilayers, Journal of applied Mechanics, 79, 031019 (2012)
8. Cheng S, Bilston LE, Unconfined compression of white matter, Journal of Biomechanics, 40(1), 117–124 (2007).
9. El Sayed T, Mota A, Fraternali F, Ortiz M A variational constitutive model for soft biological tissues, J. Biomech. 41, 1458-1466 (2008)
10. El Sayed T, Gurses E, Fraternali F, Ortiz M, A phenomonological constitutive model of finite viscoelasticity, viscoplasticity and tensile damage in polymers, submitted
11. Filas BA, Xu G, Taber LA, Mechanisms of brain morphogenesis, in Computer Models in Biomechanics, Holzapfel GA, Kuhl E (eds), pp. 337–349, (2013)
12. Gasser TC, Ogden RW, Holzapfel GA, Hyperelastic modelling of arterial layers with distributed collagen fiber orientations, Journal of the Royal Society Interface 3(6) 15-35 (2006)
13. Geng G, Johnston LA and Yan E, Britto JM, Smith DW, Walker DW, Egan GF, Biomechanisms for modelling cerebral cortical folding, Medical image analysis, 13(6) 920-930 (2009)
14. Goriely A, Vandiver R On the mechanical stability of growing arteries, IMA Journal of Applied Mathematics 75(4), 549–570 (2010)
15. Goriely A, Tabor M, Spontaneous Rotational Inversion in Phycomyces, Phys. Rev. Lett. 106, 138103 (2011).
16. Goriely A, Tabor M, Rotation, inversion and perversion in anisotropic elastic cylindrical tubes and membranes, Proc. Roy. Soc A 256, 2153 (2013)
17. Goriely A, van Dommelen JAW, Geers MGD, Holzapfel G, Jayamohan J, Jérusalem A, Sivaloganathan S, Squier W, Waters S, Kuhl E, Mechanics of the Brain: Perspectives, Challenges, and Opportunities. http://link.springer.com/article/10.1007/s10237-015-0662-4
18. Guo ZY, Peng XQ, Moran B, A composites-based hyperelastic constitutive model for soft tissue with application to the human annulus fibrosus, J. Mech. Phys. Solids 54(9), 1952-1971 (2006)
19. Hilgetag CC, Barbas H, Role of Mechanical Factors in the Morphology of the Primate Cerebral Cortex, PLOS Computational Biology 2(3): e22 (2006).
20. Holzapfel GA, Gasser TC, and Ogden RW, A new constitutive framework for arterial wall mechanics and a comparative study of material models, Journal of Elasticity and the Physical Science of Solids 61(1-3) 1-48 (2000)
21. Hong W, Zhao X, Suo Z, Formation of creases on the surfaces of elastomers and gels, Applied Physics Letters, 95(11) (2009)
22. Jin L, Cai S, Suo Z, Creases in soft tissues generated by growth, Europhysics Letters, 95(6), 64002 (2011)
23. Budday S, Kuhl E, and Hutchinson JW, Period-doubling and period-tripling in growing bilayered systems Philosophical Magazine, 1–17, 2015. DOI:10.1080/14786435.2015.1014443
24. Reese S, Govindjee S, A theory of finite viscoelasticity and numerical aspects, International Journal of Solids and Structures 35(26), 3455-3482 (1998)
25. Sun J-Y, Xia S, Moon M-W, Oh KH, Kim K-S, Folding wrinkles of a thin stiff layer on a soft substrate, Proc. Roy. Soc. A 468, 932-953 (2012)
26. van Essen, DC, A tension-based theory of morphogenesis and compact wiring in the central nervous system, Nature, 313-318 (1997).
27. Weiss JA, Gardiner JC, Computational modeling of ligament mechanics, Critical Reviews in Biomedical Engineering, 29(3) (2001)
28. Wu Z, Bouklas N and Huang R, Swell-induced surface instability of hydrogel layers with material properties varying in thickness direction, International Journal of Solids and Structures 50, 578-587 (2013).
29. Xu G, Knutsen AK, Dikranian K, Kroenke CD, Bayly PV, Taber LA, Axons pull on the brain, but tension does not drive cortical folding, Journal of Biomechanical Engineering, 132(7), 071013 (2010)
30. Zang, J, Zhao, X, Cao Y and Hutchinson, JW, Localized ridge wrinkling of stiff films on compliant substrates, J. Mech. Phys. Solids 60, 1265-1279 (2012)
31. Zheng J, Lamoureux P, Santiago V, Dennerll T, Buxbaum RE, Heidemann SR, Tensile regulation of axonal elongation and initiation, The Journal of Neuroscience, 11(4), 1117-1125 (1991)